

# Numerical Simulation of Axial Inflow Characteristics and Aerodynamic Noise in a Large-Scale Adjustable-Blade Fan

Lin Wang<sup>1</sup>, Chunguo An<sup>2</sup>, Nini Wang<sup>2</sup>, Yaming Ping<sup>1</sup>, Kun Wang<sup>1</sup>, Ming Gao<sup>1,\*</sup> and Suoying He<sup>1</sup>

<sup>1</sup>School of Energy and Power Engineering, Shandong University, Jinan, 250061, China

<sup>2</sup>Shandong Electric Power Engineering Consulting Institute Co., Ltd., Jinan, 250013, China

\*Corresponding Author: Ming Gao. Email: gm@sdu.edu.cn

Received: 08 January 2020; Accepted: 16 March 2020

**Abstract:** Numerical simulation are conducted to explore the characteristics of the axial inflow and related aerodynamic noise for a large-scale adjustable fan with the installation angle changing from  $-12^\circ$  to  $12^\circ$ . In such a range the maximum static (gauge) pressure at the inlet changes from  $-2280$  Pa to  $382$  Pa, and the minimum static pressure decreases from  $-3389$  Pa to  $-8000$  Pa. As for the axial intermediate flow surface, one low pressure zone is located at the junction of the suction surface and the hub, another is located at the suction surface close to the casing position. At the outlet boundary, the low pressure is negative and decreases from  $-1716$  Pa to  $-4589$  Pa. The sound pressure level of the inlet and outlet noise tends to increase monotonously by  $11.6$  dB and  $7.3$  dB, respectively. The acoustic energy of discrete noise is always higher than that of broadband noise regardless of whether the inlet or outlet flow surfaces are considered. The acoustic energy ratio of discrete noise at the inlet tends to increase from  $0.78$  to  $0.93$ , while at the outlet it first decreases from  $0.79$  to  $0.73$  and then increases to  $0.84$ .

**Keywords:** Adjustable blade axial flow fan; variable installation angle condition; axial static pressure; aerodynamic noise

## 1 Introduction

The adjustable-blade fans have great advantages of simple structure, strong adaptability, high efficiency and energy saving [1] in national production fields such as pipeline ventilation and forced draft fan for boilers, but the complicated axial inflow characteristics and serious noise problem always make severely effect on the producers and workers [2–4]. According to research, the noise of axial fan basically includes aerodynamic noise, electromagnetic noise and mechanical vibration noise. Among them, the aerodynamic noise accounts for the majority [5].

For inflow characteristics, Ye et al. simulated the inflow characteristics of single moving blades, adjacent and interphase moving blades when the installation angle is abnormal, and obtained the effects of the abnormal blades, deviation and phase on performance [6–8]. Subsequently, Ye et al. performed a three-dimensional simulation of the two-stage adjustable-blade fan, and obtained the effects of the first and second impellers on the internal flow characteristics [9,10].



This work is licensed under a Creative Commons Attribution 4.0 International License, which permits unrestricted use, distribution, and reproduction in any medium, provided the original work is properly cited.

There are usually two methods to study aerodynamic noise, numerical simulation and experimental research. In terms of numerical simulation, Hake predicted noise source by large eddy simulation (LES), unsteady Reynolds average N-S simulation (URANS), detached eddy simulation (DES), and scale-adaptative simulation (SAS) [11]. Hu et al. performed the numerical simulation to study the noise caused by dynamic and static interference, and found that the boundary element method can effectively improve the accuracy [12]. Pang et al. studied the discrete noise sound pressure level through the FW-H model, and found that the discrete noise caused by front stage moving blade was the main component of total [13]. Otherwise, Zhai et al. [14] studied the noise experimentally at the inlet and outlet, and obtained that different materials should be used to reduce the spectral noise. Yang et al. used a semicircular microphone and a nonuniformly linear microphone to measure the noise, and obtained the distribution of noise source at the inlet and outlet [15].

In response to noise reduction, Ma proposed a micro-perforated plate to absorb the sound by resonance, and then made further research on the work of noise reduction [16,17]. Since then, many scholars such as Zhang et al. [18], Wu et al. [19], Zhang et al. [20], Qian et al. [21] have conducted more deeply on this technology, and found the efficient way to reducing noise by micro-perforation structure. In addition, Liu et al. [22] conducted experiments and numerical simulations to study different inclination angles of static blade, and found that the static blade tilting can effectively reduce the peak frequency caused by dynamic and static interference.

Thus, based on the three-dimensional geometric model for large-scale adjustable-blade axial fan, this paper firstly studied the internal inflow field, then analyzed the relationship between installation angle and the sound pressure level, finally researched the spectral characteristics for the inlet and outlet noise. This study has a great significance on the development of high performance and low aerodynamic noise of adjustable axial-flow fan, and can lay the foundation for the investigation of noise reduction measures.

## 2 Numerical Simulation

### 2.1 Geometric Model

This study focuses on the adjusted axial-flow fan of one 660 MW supercritical coal-fired unit. The impeller rotation speed is 990 r/min. The blade structural parameters and shell structure parameters of the fan are shown in Tab. 1.

In order to ensure the precision requirements of the study, the movable blade model which is built by three-dimensional scanning technology is shown in Fig. 1.

**Table 1:** Blade structural parameters and shell structure parameters

Project	Unit	Numerical value
Diameter of impeller	mm	2628
Tip clearance	mm	4
Blade bottom chord length	mm	285
Blade top chord length	mm	248
Number of moving blades	sheet	22
Fan speed	r/min	990
Impeller number	level	1
Flare inlet diameter	mm	3250
Diffusion tube outlet diameter	mm	3550



**Figure 1:** Dynamic blade model

Additionally, the two-dimensional and overall three-dimensional geometric model are shown in [Figs. 2](#) and [3](#). The inlet and outlet section are extended to ensure fully developed flow in pipes, which can increase the simulation's accuracy and convergence [\[23\]](#).

### 3 Mathematical Models and Calculation Methods

The air flow inside the fan is turbulent and viscous. It is known that the mechanical energy is converted into the kinetic and potential energy of the air flow in the fan. Since the temperature of the air flow remains essentially constant, and the heat exchange of the air flow is so small that it can be ignored. Therefore, only the mass conservation equation and the momentum conservation equation are calculated, and the momentum conservation equation is closed by the standard  $k-\varepsilon$  turbulence model. The calculation of the sound field mainly focuses on the aerodynamic noise generated by the internal turbulent airflow, so the FW-H equation is used in this study.

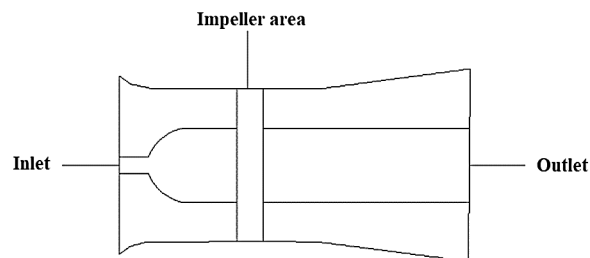


**Figure 2:** Inlet and outlet section

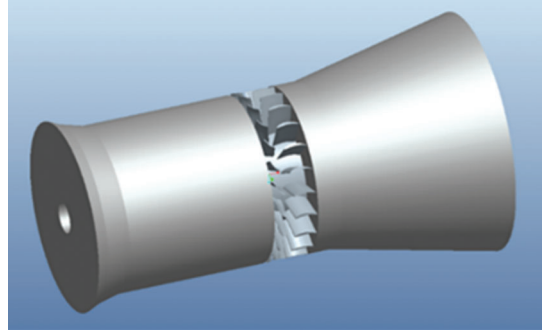


**Figure 3:** Three-dimensional geometric model

### 3.1 Standard $k$ - $\epsilon$ Model

In this paper, the Standard  $k$ - $\epsilon$  model is selected as the turbulence model for steady state simulation. It has the advantages of stability, economy and high accuracy. The transport equations are as follows,

$$\frac{\partial(\rho k \mu_i)}{\partial x_i} = \frac{\partial}{\partial x_j} \left[ \left( \mu + \frac{\mu_t}{\sigma_k} \right) \frac{\partial k}{\partial x_j} \right] + P_k - \rho \epsilon \quad (1)$$

$$\frac{\partial(\rho \epsilon \mu_i)}{\partial x_i} = \frac{\partial}{\partial x_j} \left[ \left( \mu + \frac{\mu_t}{\sigma_\epsilon} \right) \frac{\partial \epsilon}{\partial x_j} \right] + \frac{\epsilon}{k} (c_1 P_k - c_2 \rho \epsilon) \quad (2)$$

where  $k$  is the turbulent kinetic energy, J;  $\epsilon$  represents the turbulent dissipation rate, %;  $\mu_t$  stands for the turbulent viscosity, Pa·s;  $P_k$  is the pressure generation term caused by the velocity gradient, Pa.

The SIMPLE algorithm is selected to couple the pressure and speed, and the parameters of each aerodynamic performance are set to second-order upwind. All the walls are set as non-slip boundaries, and the turbulent intensity and hydraulic diameter can be written by,

$$I = 0.16 Re^{-\frac{1}{8}} \quad (3)$$

$$D = \frac{4(\pi R_{in}^2 - \pi r_{in}^3)}{2\pi(R_{in} + r_{in})} \quad (4)$$

where  $Re$  is the Reynolds number of the fluid;  $R_{in}$  is the entrance radius, mm;  $r_{in}$  is the entrance hub radius, mm.

### 3.2 FW-H Equation

Ffowcs Williams and Hawkins extended Curle's method to moving objects in fluid by using generalized function method, and derived the famous FW-H equation [24,25]. FW-H equation can accurately describe the sound problem caused by the interaction between fluid and moving objects, which is a kind of inhomogeneous sound wave equation based on the N-S equation [26], it was expressed as follows,

$$\begin{aligned} \frac{1}{a_0^2} \frac{\partial^2 p'}{\partial t^2} - \nabla^2 p' = & \frac{\partial}{\partial t} \{ [\rho_0 v_n + \rho(u_n - v_n)] \delta(f) \} \\ & - \frac{\partial}{\partial x_i} \{ [p_{ij} n_j + \rho u_i (u_n - v_n)] \delta(f) \} + \frac{\partial^2}{\partial x_i \partial x_j} \{ T_{ij} H(f) \} \end{aligned} \quad (5)$$

where  $a_0$  is the speed of sound in air, m/s,  $p'$  is the far-field pressure, Pa,  $\rho_0$  is the reference density of the fluid,  $f$  is the surface,  $v_n$  is the surface velocity normal to the surface  $f$ , m/s,  $u_n$  is the flow velocity

component to the surface  $f$ , m/s,  $v_i$  is the surface velocity component in the  $x_i$  direction, m/s,  $u_i$  is the flow velocity component in the  $x_i$  direction, m/s,  $n_j$  is the unit normal vector,  $\delta(f)$  is the Dirac Delta function,  $H(f)$  is the Heaviside function,  $p_{ij}$  is the stress tensor,  $T_{ij}$  is the Lighthill stress tensor.

The numerical simulation of aerodynamic noise is mainly guided by the FW-H equation, and combined with CFD software. The simulation process could be divided into two steps. The first step is to obtain the unsteady flow characteristics by LES turbulence model because of small-scale vortices with strong randomness, and the pre-converged steady flow field obtained is adopted as the initial condition. The second step is choosing the sound source surface and setting noise monitoring point. The calculation is considered to be convergent when the residual value is less than  $1 \times 10^{-3}$ . The number of calculation step is 720 steps, and the time step is described as follows,

$$\Delta t = \frac{60}{nK} \quad (6)$$

where  $K$  is the step number in a rotational period of the impeller (= 360 in the study), and  $n$  is the rotational speed (= 990 r/min in the study),  $\Delta t$  is  $1.6835 \times 10^{-4}$  s in the study.

### 3.3 Meshing and Independence Verification of Fluid Domain

Based on ICEM CFD, the tetrahedral grid is used for the bell mouth, the outlet guide vane, and the diffuser tube, and the hexahedral grid is used for the moving impeller and tip clearance, as shown in Fig. 4. Additionally, the detail of impeller is shown in Fig. 5.

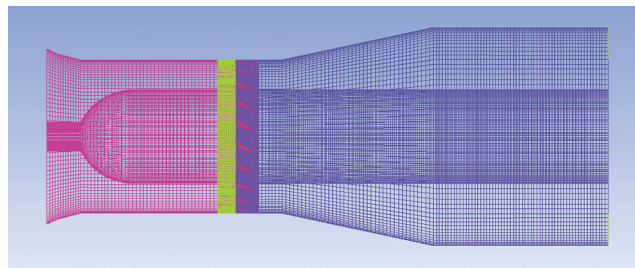


**Figure 4:** Overall grid diagram of the axial-flow fan

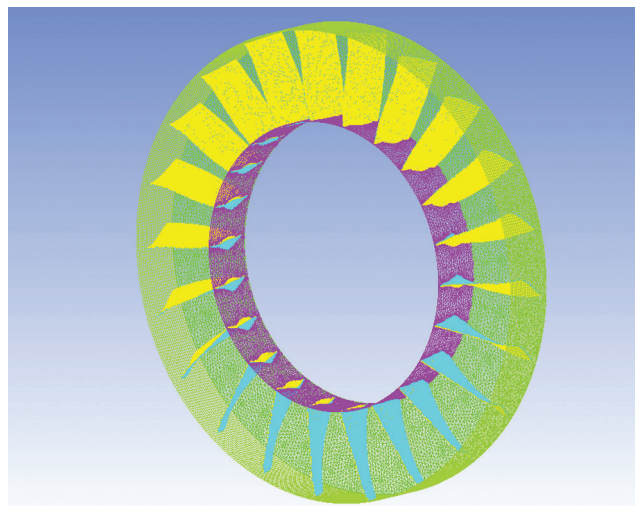


**Figure 5:** Dynamic impeller area grid diagram

By comparing the design value and real value of the outlet total pressure, four kinds of grid independence are verified, as 480 million, 510 million, 550 million and 600 million, as shown in Tab. 2.

Tab. 2 shows that the relative errors are within reasonable range except Grid 1 and relative error between Grid 3 and Grid 4 is substantially negligible, taking account about the computational time and costs [27], so the 550 million grid number is chosen to conduct the research.

**Table 2:** Grid independence analysis

	Number of grids/10,000	Outlet total pressure/Pa	Relative error
Grid 1	480	4583	5.3%
Grid 2	510	4551	4.5%
Grid 3	550	4532	4.1%
Grid 4	600	4529	4.0%

### 3.4 Model Validation

#### 3.4.1 Flow Field Model Validation

The accuracy of the model can be validated by comparing the simulated and designed values of the outlet total pressure in five operating conditions, as shown in Fig. 6.

It can be seen from Fig. 6 that the simulation value is always higher than the design value. On the one hand, the number of meshes impacts the simulation result, when the number of meshes is sufficiently large, the simulation value will approach the design value. On the other hand, numerical simulation performs a partial simplified assumption, so it can not completely fit the actual situation. However, the trend of the simulation results is consistent with the design value, and the maximum relative error is about 3.7%, which is within the allowable range.

#### 3.4.2 Sound Field Model Verification

The sound pressure level (SPL) is expressed as follows,

$$SPL = 10 \lg \frac{p_e^2}{p_{ref}^2} \quad (7)$$

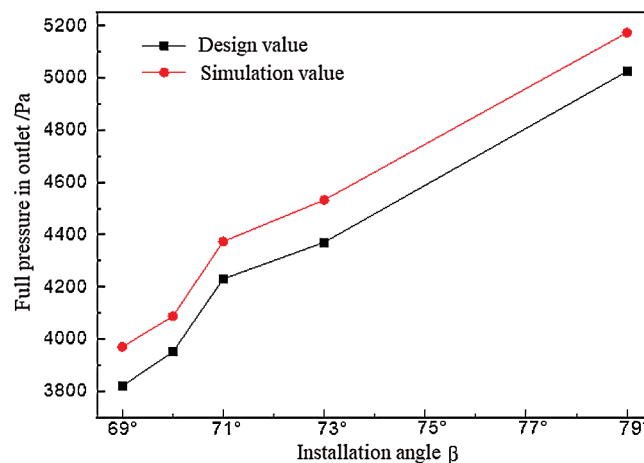


**Figure 6:** Comparison of design value with simulation value

where  $P_{ref}$  is the reference sound pressure ( $= 2 \times 10^{-5}$  Pa in air), and  $P_e$  is the effective value of acoustic pressure define as,

$$P_e = \sqrt{\frac{1}{T} \int_0^T p'^2 dt} \quad (8)$$

The Fast Fourier Transform is used to convert the sound pressure pulsation in the time domain to that in the frequency domain. Taking the simulation results of rated conditions as an example, the sound spectra is shown in the Fig. 7.

It can be seen from Fig. 7 that the discrete noise peaks appear at the fundamental frequency of 363 Hz, and the peaks gradually decrease. The simulation results are roughly similar to the literature [28], which qualitatively validates the correctness of the acoustic calculation model.

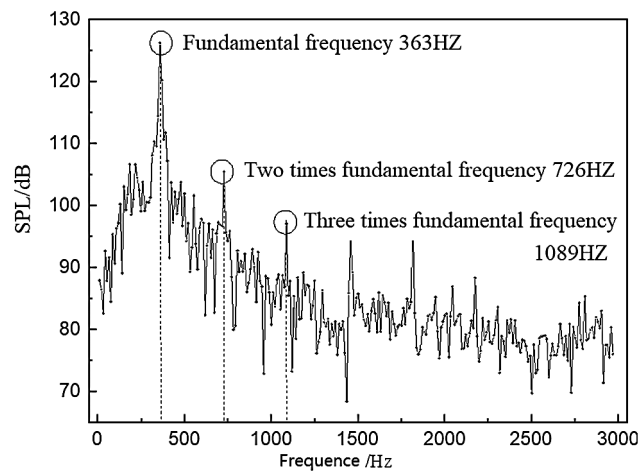


Figure 7: The sound spectra

## 4 Results and Discussion

### 4.1 Calculation Analysis of Radial Pressure at Different Installation Angle

The installation angle is defined as the angle between the moving blade chord and the opposite direction of the impeller circumferential partial velocity, as shown in Fig. 8.

The installation angle of the blade in the rated state is  $73^\circ$ , and the positive deflection is the blade rotating counterclockwise along the airfoil axis. According to the general performance curve of the axial fan, there are seven angles are researched in this study, including  $\Delta\beta = 0^\circ, \pm 4^\circ, \pm 8^\circ$  and  $\pm 12^\circ$  respectively.

The pressure contours of three flow channels taken along the axial direction of the impeller are defined as section D, E, and F. The Section D is the impeller inlet flow surface, the section E is the impeller axial intermediate flow surface (50% of the impeller axial length position), and the section F is the impeller outlet flow surface, as shown in Fig. 9.

The Section D is the axial inlet surface where the air flow will enter the rotation region and impinge the blades transforming the airflow to turbulent. As the blade tip separates the vortex, high pressure is generated at the inner wall of the casing, as shown in Fig. 10.

It can be seen from the Fig. 10 that, as the installation angle varies from  $-12^\circ$  to  $12^\circ$ , the maximum static pressure changes from  $-2280$  Pa to  $382$  Pa, and the minimum static pressure decreases from  $-3389$  Pa to  $-8000$  Pa. What's more, the maximum value and the minimum value of static pressure appear in the

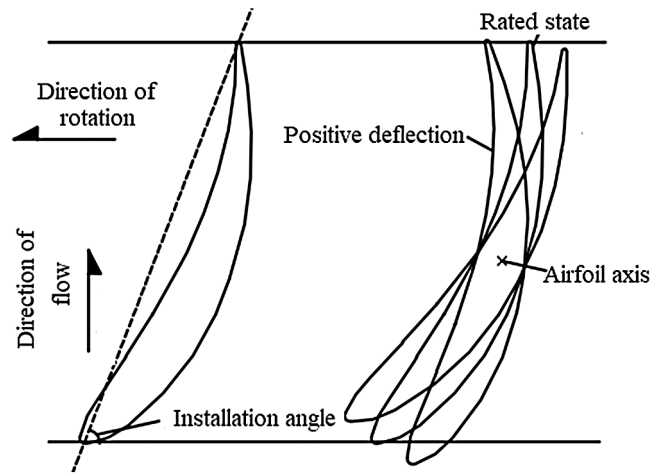


**Figure 8:** The plan view of installation angle

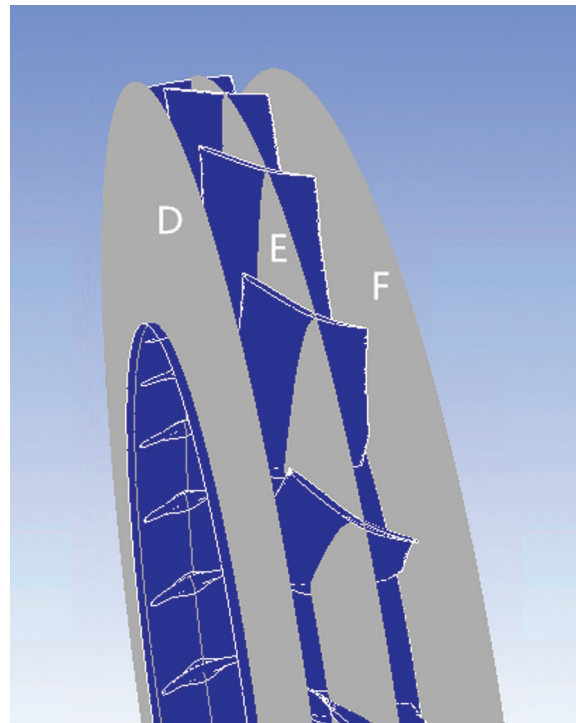


**Figure 9:** Axial characteristic sections

operating condition  $\Delta\beta = 12^\circ$ , and the minimum value is located in the position close to the blade leading edge surface of the hub.

The Section E is the axial center surface of the impeller. The pressure surface and suction surface are shown in Fig. 11.

As Fig. 11 shows, the high static pressure zone is located at the pressure surface near the top of the blade, because the turbulence reduces static pressure caused by viscous forces near the surface of the casing. Due to the tip clearance, the airflow is forced to flow through the gap to the adjacent flow channel, thereby

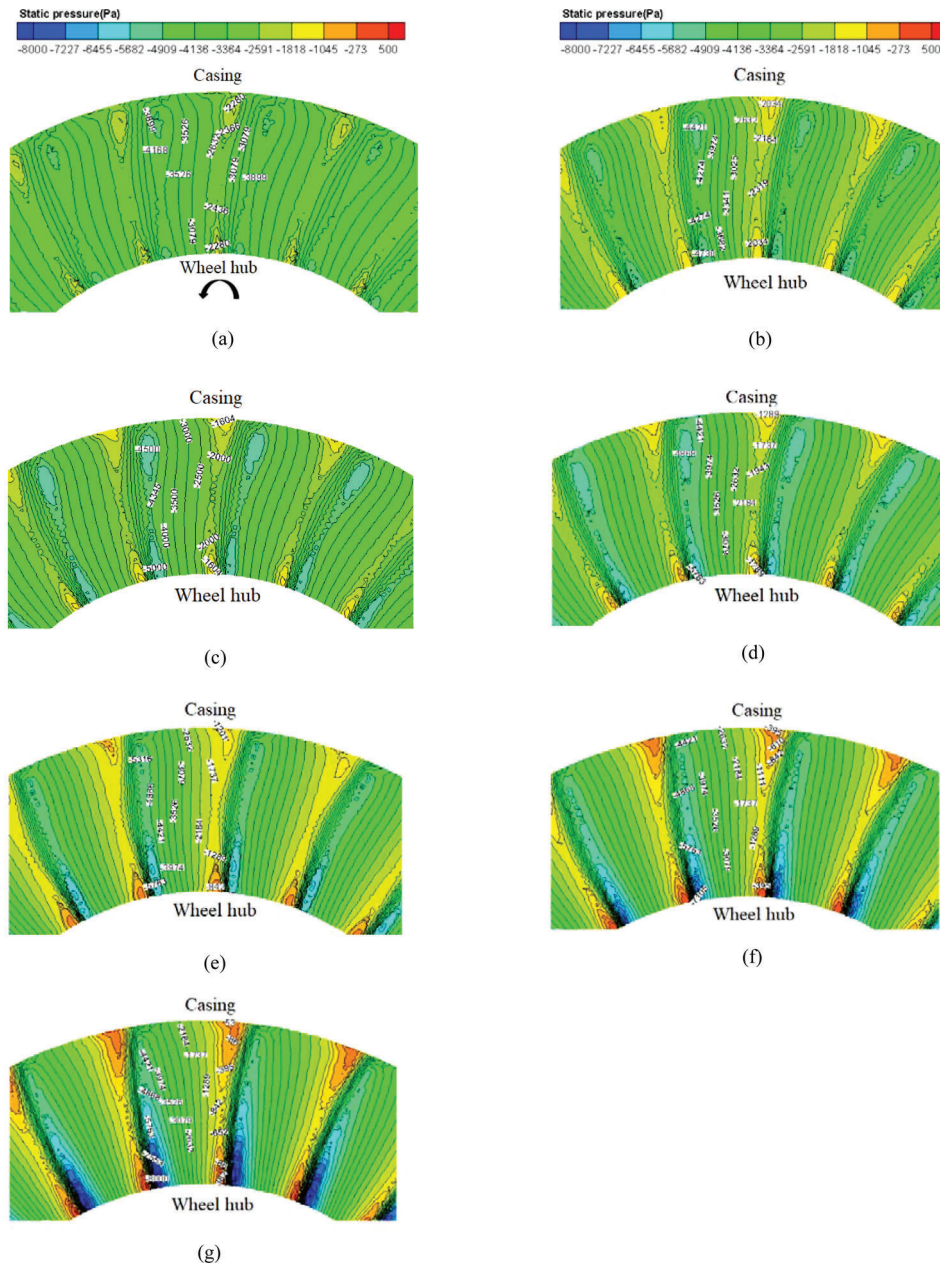


**Figure 10:** Cloud map of static pressure distribution on Section D. (a)  $\Delta\beta = -12^\circ$  (b)  $\Delta\beta = -8^\circ$  (c)  $\Delta\beta = -4^\circ$  (d)  $\Delta\beta = 0^\circ$  (e)  $\Delta\beta = 4^\circ$  (f)  $\Delta\beta = 8^\circ$  and (g)  $\Delta\beta = 12^\circ$

destroying the mainstream flow and generating the lower negative pressure. There are two low-pressure areas on the suction surface. The first is the interface between the suction surface and the hub, and the second is the location close to the casing at the suction surface due to the gap between the blade tips. Comparing the pressure values, it can be seen that the maximum static pressure increases from 3895 Pa to 4895 Pa, the maximum static pressure difference between adjacent conditions is between 10 Pa and 300 Pa, and the minimum static pressure first increases from  $-4395$  Pa to  $-3842$  Pa and then decreases to  $-50000$  Pa.

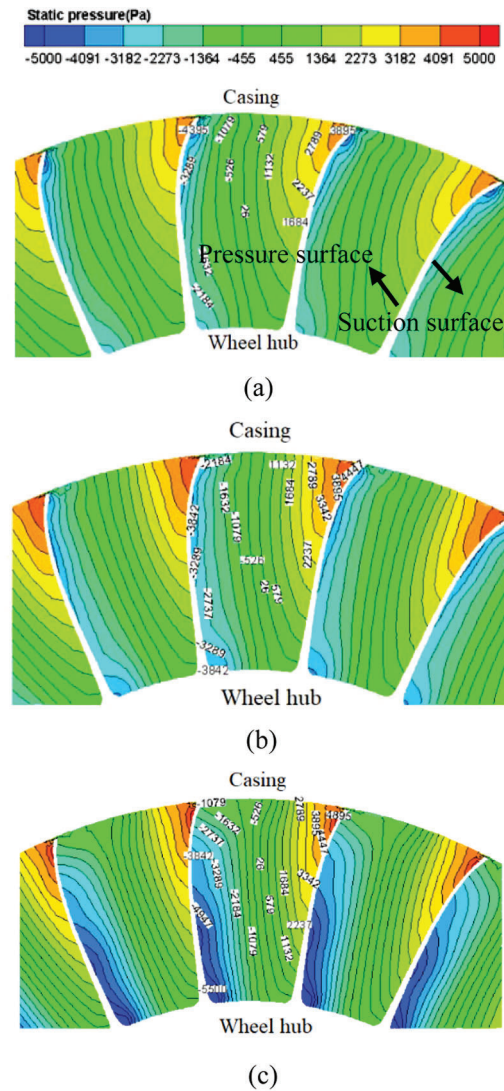


**Figure 11:** Cloud map of static pressure distribution on Section E. (a)  $\Delta\beta = -12^\circ$  (b)  $\Delta\beta = 0^\circ$  and (c)  $\Delta\beta = 12^\circ$

The Section F is the axial outlet surface of the impeller, and the high-pressure zone and the low-pressure zone are alternately distributed, as shown in Fig. 12.

It can be seen from the Fig. 12 that the high-pressure zone is located near the 90% channel height, while the low pressure zone is near 45% of the runner height. The low pressure is negative and decreases from  $-1716$  Pa to  $-4589$  Pa with the changing of the installation angle.

Additionally, there are sixteen sections uniformly intercepted from the inlet to the outlet of the impeller. The inlet flow surface is defined as  $0$  mm, and the outlet flow surface is  $310$  mm. The position of any axial flow surface is represented by  $D_L$ , and the static pressure value of each monitoring surface is calculated as shown in Fig. 13.

According to the Fig. 13, the flow channel can be divided into three parts, the part L1 is  $D_L = 0$  mm to  $D_L = 40$  mm, where the static pressure is gradually reduced. The part L2 is  $D_L = 40$  mm to  $D_L = 280$  mm, where the static pressure first increases and then decreases, and the turning point position gradually moves toward

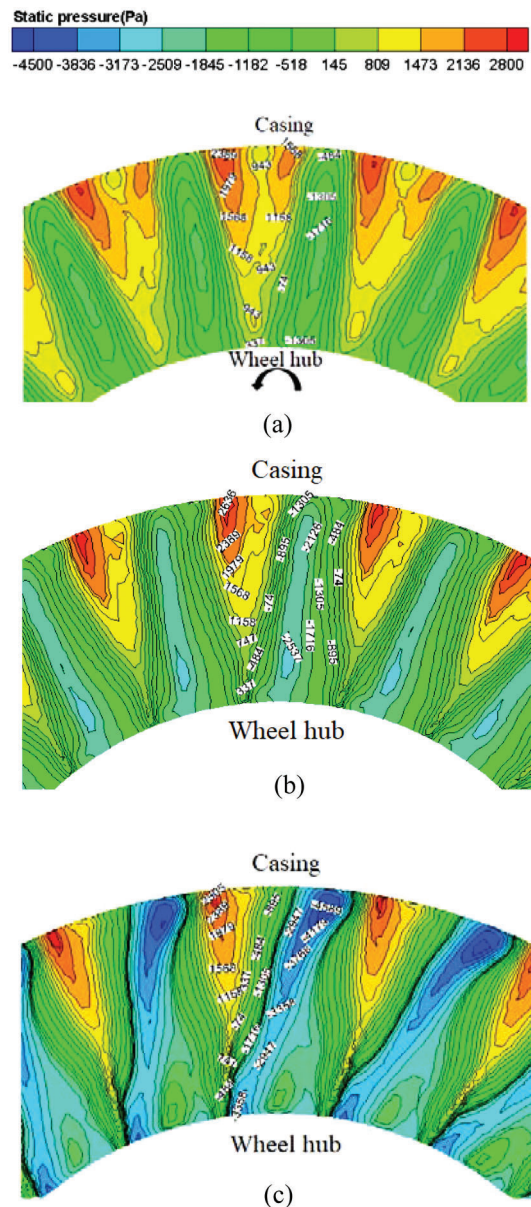


**Figure 12:** Cloud map of static pressure distribution on Section F. (a)  $\Delta\beta = -12^\circ$  (b)  $\Delta\beta = 0^\circ$  and (c)  $\Delta\beta = 12^\circ$

the outlet. The part L3 is  $D_L = 280$  mm to  $D_L = 310$  mm, where the static pressure smoothly increases. The reason for the increase in the part L2 is that the blade works on the gas, so that the dynamic pressure is continuously converted into static pressure. The decrease happens because the trailing edge of the blade is worn near the top position, and the effect of supercharging is not totally achieved. The damage position gradually approaches the impeller outlet with the increase of the installation angle, so the turning point in L2 gradually moves toward the impeller outlet.

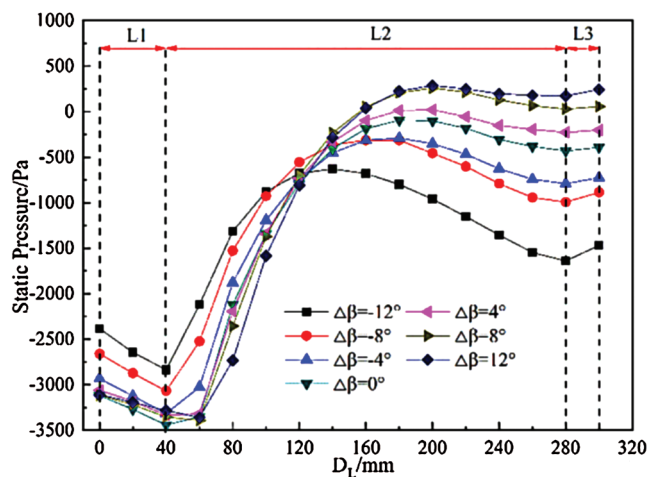


**Figure 13:** Axial static pressure curve under different installation angles

## 4.2 Sound Simulation of Inlet and Outlet at Different Installation Angle

### 4.2.1 Noise Source and Monitoring Point Settings

The sound simulation is based on FW-H equation, of which the selection of noise source is the most important. The noise source of the whole fan can be divided into the casing surface and the impeller surface. This study compares the calculation of the casing, the impeller, and the casing & impeller to propose the contribution of different sound sources. The calculation results are shown in [Tab. 3](#).

**Table 3:** Comparison of calculation results of different sound source surfaces

Sound source surface	Inlet monitoring point/dB	Exit monitoring point/dB
Casing	123.46	110.85
Impeller	93.63	95.54
Casing & impeller	124.10	111.62

It can be seen from [Tab. 3](#) that the casing is the main source of noise, but the impact of the impeller surface cannot be ignored either, so the subsequent calculations chooses the casing & impeller as the overall sound source.

According to GBT288-91, the noise monitoring points in the horizontal position are set as shown in [Fig. 14](#).

### 4.2.2 SPL

The inlet and outlet noise level are monotonic increasing, and the inlet noise is greater than that of outlet, as shown in [Fig. 15](#).

As it can be seen from the [Fig. 15](#), for the aerodynamic noise of inlet, as  $\Delta\beta$  deflects from  $-12^\circ$  to  $12^\circ$ , the sound pressure level increases by 11.6 dB. Among them, as  $\Delta\beta$  turns from  $-12^\circ$  to  $-8^\circ$ , the sound pressure level changes the most, increasing by 3.4 dB, accounting for 29.6% of the total change. Under other working conditions, the sound pressure level increases by 1–2 dB with every  $4^\circ$  increase in installation angle. For the aerodynamic noise of outlet, as  $\Delta\beta$  turns from  $-12^\circ$  to  $12^\circ$ , the sound pressure level increases by 7.3 dB. Among them, as  $\Delta\beta$  deflects from  $-12^\circ$  to  $-8^\circ$ , the sound pressure level

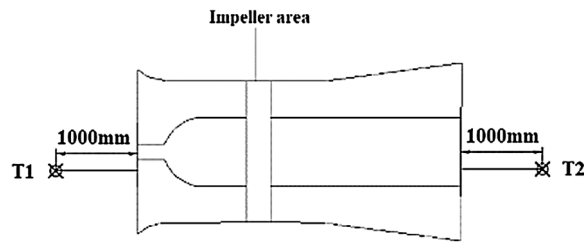


Figure 14: Monitoring points disposed of inlet and outlet

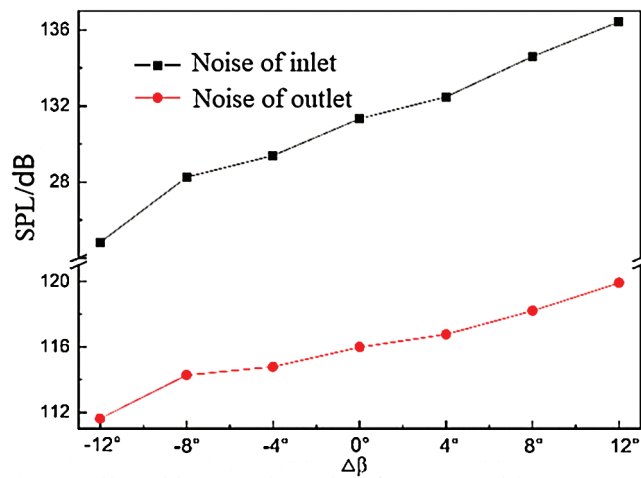


Figure 15: Sound pressure level curve of inlet and outlet noise

changes the most, increasing by 2.7 dB, accounting for 36.4% of the total change. Under other working conditions, the sound pressure level increases by 0.5–1.5 dB with every 4° increase in installation angle.

#### 4.2.3 The Proportion of Noise Energy

The average acoustic energy per unit volume is adopted to analyze the frequency distribution characteristics of the noise, the expression is,

$$\epsilon = \frac{p_e^2}{\rho_0 c_0^2} \tag{9}$$

where  $p_e$  is effective sound pressure, Pa;  $\rho_0$  is the air density, kg/m<sup>3</sup>,  $c_0$  is the speed of sound, m/s.

The ratio of the acoustic energy density to the total acoustic energy density at a certain frequency is defined as the acoustic energy ratio  $C_{pi}$ , its expression is as follows,

$$C_{pi} = \frac{\epsilon_i}{\epsilon_{total}} \tag{10}$$

$$C_p = \sum_n^i \frac{\epsilon_i}{\epsilon_{total}} \tag{11}$$

According to the sound pressure level in Fig. 7 and Eqs. (9)–(11), the acoustic energy density and the ratio of acoustic energy at any frequency can be calculated. It can be observed that, at any mounting angle condition, most of the acoustic energy is concentrated in the low frequency band 20–500 Hz. Therefore, the frequency band of aerodynamic noise is divided into two band, the discrete noise and wideband noise. The

frequency of the discrete noise includes the blade passing frequency and its multiples. The frequency of the wideband noise is all remaining frequencies.

The histograms of sound energy ratio of inlet noise and outlet noise are shown in Figs. 16 and 17. It can be found that the acoustic energy density of discrete noise is higher than that of broadband noise.

It can be seen from the Fig. 16 that with the changing of the installation angle, the acoustic energy ratio of the discrete noise in inlet noise increases constantly, the ratio increases from 0.78 to 0.93, in contrast, broadband noise continues to decrease. As for outlet noise in Fig. 17, the acoustic energy ratio of discrete noise decreases from 0.79 to 0.73 and then increases to 0.84 with  $\Delta\beta = 0^\circ$  as the turning point.

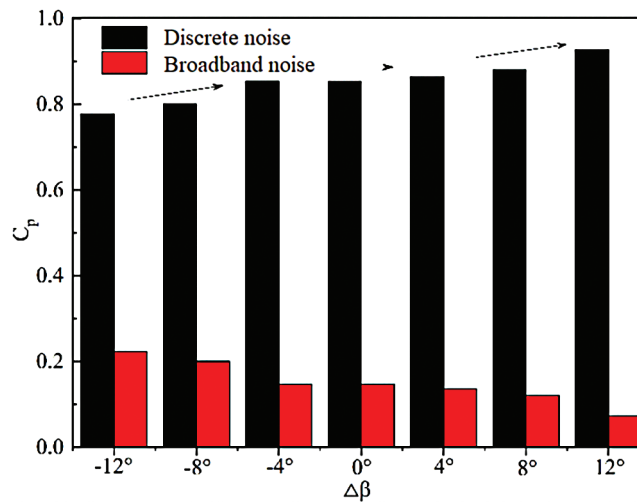


Figure 16: The proportion of inlet noise energy

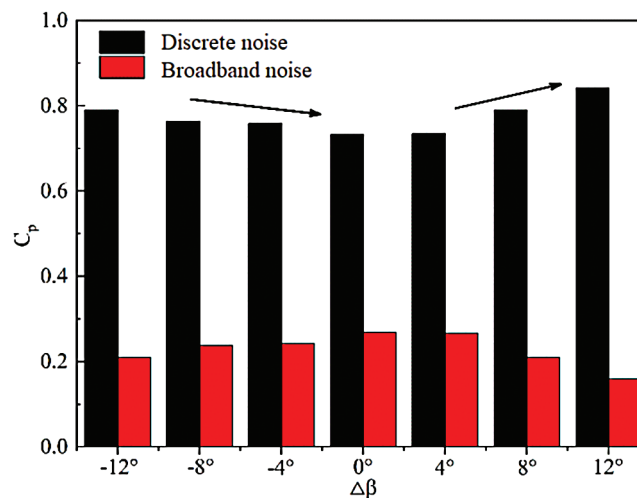


Figure 17: The proportion of outlet noise energy

## 5 Conclusions

(1) With the installation angle  $\Delta\beta$  varying from  $-12^\circ$  to  $12^\circ$ , the maximum static pressure increases from  $-2280$  Pa to  $382$  Pa, the minimum static pressure decreases from  $-3389$  Pa to  $-8000$  Pa at the axial inlet flow

surface. At the axial outlet flow surface, the high-pressure zone is located near the 90% channel height, while the low-pressure zone is near 45% of the runner height. The low pressure is negative and decreases from  $-1716$  Pa to  $-4589$  Pa.

(2) As  $\Delta\beta$  changes from  $-12^\circ$  to  $12^\circ$ , the maximum static pressure increases from  $3895$  Pa to  $4895$  Pa, and the maximum static pressure difference between adjacent conditions is between  $10$  Pa and  $300$  Pa, and the minimum static pressure is increased from  $-4395$  Pa to  $-3842$  Pa and then decreases to  $-5500$  Pa.

(3) The sound pressure level changes the most when  $\Delta\beta$  changes from  $-12^\circ$  to  $-8^\circ$ , and the inlet noise increases by  $3.4$  dB, accounting for  $29.6\%$  of the total change. Under other working conditions, the sound pressure level increases by  $1\text{--}2$  dB with every  $4^\circ$  increase in installation angle. The outlet noise increases by  $2.7$  dB, accounting for  $36.4\%$  of the total change, except that, the sound pressure level increases by  $0.5\text{--}1.5$  dB. What's more, the acoustic energy ratio of inlet discrete noise increases from  $0.78$  to  $0.93$ . The acoustic energy ratio of outlet discrete noise, with  $\Delta\beta = 0^\circ$  as the turning point, decreases from  $0.79$  to  $0.73$  and then increases to  $0.84$ .

**Acknowledgement:** This paper is supported by Key Research and Development Project of Shandong Province (2019GSF109084) and Young Scholars Program of Shandong University (2018WLJH73).

**Funding Statement:** This work was supported by Key Research and Development Project of Shandong Province [2019GSF109084] and Young Scholars Program of Shandong University [2018WLJH73].

**Conflicts of Interest:** The authors declare that they have no conflicts of interest to report regarding the present study.

## References

1. He, C., Guo, L. J. (2008). *Pump and fan*. China Electric Power Press.
2. Zhang, Y. C., Yi, D. L., Feng, D. Y., Liu, S. H. (2011). *Design and selection of ventilator*. Beijing: Chemical Industry Press.
3. Banbury, S. P., Berry, D. C. (2005). Office noise and employee concentration: identifying causes of disruption and potential improvements. *Ergonomics*, *48*(1), 25–37. DOI 10.1080/00140130412331311390.
4. Li, Y., Liu, J., Ouyang, H., Du, Z. H. (2008). Internal flow mechanism and experimental research of low-pressure axial fan with forward-skewed blades. *Journal of Hydrodynamics*, *20*(3), 299–305. DOI 10.1016/S1001-6058(08)60061-X.
5. Zuo, S. G., Hu, Q., Han, H. J., Kang, Q. (2014). Analysis of the effect of blade thickness on blade noise of vortex fan. *Vibration and Shock*, *33*(8), 130–147.
6. Ye, X. M., Li, J., Li, C. X., Wang, S. L. (2010). Inflow characteristics and operating characteristics of axial fan with multiple moving blade mounting angles under asynchronous adjustment. *Chinese Journal of Electrical Engineering*, *30*(32), 77–83.
7. Ye, X., Li, P., Li, C., Ding, X. (2015). Numerical investigation of blade tip grooving effect on performance and dynamics of an axial flow fan. *Energy*, *82*, 556–569. DOI 10.1016/j.energy.2015.01.065.
8. Ye, X. M., Li, J., Wang, S. L., Li, C. X., Qian, H. W. (2009). Aerodynamic characteristics of moving blade adjustable axial fan with abnormal installation angle of blade. *Chinese Journal of Electrical Engineering*, *29*(26), 79–84.
9. Ye, X. M., Li, X. Y., Li, C. X. (2013). Numerical simulation of the inflow characteristics of a two-stage moving blade adjustable axial fan. *Chinese Journal of Power Engineering*, *33*(11), 871–877.
10. Ye, X. M., Li, X. Y., Li, C. X. (2014). Effect of first-stage guide blade improvement on performance of two-stage moving blade adjustable axial fan. *Chinese Journal of Power Engineering*, *34*(3), 228–235.

11. Reese, H., Carlous, T., Kato, C. (2007). Numerical prediction of the aerodynamic sound sources in a low-pressure axial fan with inflow distortion. *Fan Noise*, 1–12.
12. Hu, B. B., OuYang, H., Wu, Y. D., Jin, G. Y., Qiang, X. Q. et al. (2013). Numerical prediction of the interaction noise radiated from an axial fan. *Applied Acoustics*, 74(4), 544–552. DOI 10.1016/j.apacoust.2012.09.009.
13. Pang, L., Li, S., Li, X. K. (2008). Numerical prediction of discrete noise of rotating axial fan. *Proceedings of the 21st National Conference on High Technology and Application of Vibration and Noise*.
14. Zhai, C., Tang, Z., Zou, Q., Qin, L. (2016). Experimental study on the noise characteristics regarding axial auxiliary fans and the noise reduction performance of mufflers. *Arabian Journal for Science and Engineering*, 41(12), 4817–4826. DOI 10.1007/s13369-016-2165-8.
15. Yang, Y., Wang, L. F., Yang, D. G. (2019). Noise measurement and experimental research of typical axial convection fan. *Fan Technology*, 61(2), 69–74.
16. Ma, D. Y. (1975). The theory and design of sound-absorbing structure of micro-perforated plate. *Science in China*, (1), 38–50.
17. Ma, D. Y. (1997). Accurate theory and design of sound-absorbing body of micro-perforated plate. *Journal of Acoustics*, (5), 385–393.
18. Zhang, Z. M., Gu, X. T., Shi, X., Xu, T. Y. (1989). Study on noise reduction of fan blade perforation. *Coal Mine Machinery*, (5), 1–4.
19. Wu, X. J., Li, Z. M. (2001). *Fan Technology*, (4), 11–13.
20. Zhang, B., Li, L. L., Lu, W. J. (2010). Study on sound absorption characteristics of micro-perforated plates considering the interaction between holes. *Applied Acoustics*, 29(2), 134–140.
21. Qian, H. Y. (2012). *Study on the performance and noise affecting factors of small axial fan*. China: Zhejiang University of Science and Technology.
22. Liu, H. J., OuYang, H., Tian, J., Wu, Y. D., Du, Z. H. (2013). Effect of static leaf inclination on acoustic characteristics of dynamic and static interference. *Journal of Shanghai Jiao Tong University*, 47(11), 1783–1789.
23. Tian, P., Huang, J., Shi, W., Zhou, L. (2019). Optimization of a centrifugal pump used as a turbine impeller by means of an orthogonal test approach. *Fluid Dynamics & Materials Processing*, 15(2), 139–151. DOI 10.32604/fdmp.2019.05216.
24. Williams, J. E., Hawkings, D. L. (1969). Theory relating to the noise of rotating machinery. *Journal of Sound and Vibration*, 10(1), 10–22. DOI 10.1016/0022-460X(69)90125-4.
25. Williams, J. E., Hawkings, D. L. (1969). Sound generation by turbulence and surfaces in arbitrary motion. *Philosophical Transactions of the Royal Society of London Series A-mathematical and Physical Sciences*, 264 (1151), 321–342.
26. Brentner, K. S., Farassat, F. (1998). Analytical comparison of the acoustic analogy and Kirchhoff formulation for moving surfaces. *AIAA Journal*, 36(8), 1379–1386. DOI 10.2514/2.558.
27. Cheng, X. R., Chen, H. X., Wang, X. Q. (2019). Analysis of the impact of the space guide vane wrap angle on the performance of a submersible well pump. *Fluid Dynamics & Materials Processing*, 15(3), 271–284.
28. Dong, P. X. (2016). *Numerical simulation of radiated noise of centrifugal pump based on three-dimensional flow field under variable working conditions*. China: Shandong University.